Influence of Different Silica Nanoparticles on Drop Size Distributions in Agitated Liquid-Liquid Systems

Susanne Röhl*, Lena Hohl, Maresa Kempin, Frauke Enders, Nico Jurtz, and Matthias Kraume

DOI: 10.1002/cite.201900049

Dedicated to Prof. Dr. techn. Hans-Jörg Bart on the occasion of his 65th birthday

The impact of different silica nanoparticles on rheology, interfacial tension and drop size distributions in liquid-liquid systems is determined experimentally. The particles vary in wettability and specific surface area. In contrast to commonly used high-energy devices for Pickering emulsion preparation, low energy input by stirring allows to quantify drop breakage and coalescence in steady state and dynamic conditions. The experiments can provide essential information for drop size model development in nanoparticle-stabilized emulsions.

Keywords: Coalescence, Dispersion, Drop size distribution, Endoscope, Pickering emulsion, Stirred tank

Received: February 27, 2019; *accepted:* August 23, 2019

1 Introduction

Nanoparticles can be applied as emulsifying agents to stabilize liquid-liquid systems towards coalescence (Pickering emulsions) [1, 2]. Due to the adsorption of nanoparticles at the liquid-liquid interface, coalescence is hindered or arrested, and smaller drop size distributions and a higher interfacial area can be achieved [3–5]. The higher interfacial area promotes mass transfer so that nanoparticles can be used as innovative additives for liquid-liquid reactions [6, 7]. However, the particles can also lead to an additional mass transfer resistance if they are densely packed at the liquid-liquid interface. It is crucial to understand the impact of particle characteristics such as shape, size and surface modification on their spatial arrangement at the interface, the drop size distributions and the resulting mass transfer [8]. To achieve a long-term stabilization of Pickering emulsions against coalescence, small droplet sizes are needed [9]. These are often realized by using high-energy dispersion units for emulsion preparation, such as ultrasonication or rotor-stator homogenizers. The formulation parameters and the corresponding final emulsion properties have been investigated by various authors [6, 7, 9–12]. However, for large-scale industrial applications with Pickering emulsions as innovative reaction systems, high energy consumption during emulsion preparation should be avoided in order to achieve an economically viable process. Furthermore, there still is a gap of knowledge concerning the detailed emulsification mechanisms [13].

The aim of this work is to determine the influence of different silica nanoparticles on the dynamic and steady-state drop size distributions at comparatively low energy dissipation rates induced by stirring. Therefore, an in situ endoscope measurement technique and image analysis is applied. The silica nanoparticles vary in specific particle surface area, determined via the Brunauer-Emmett-Teller (BET) method [14], and in residual silanol content, which affects the particle wettability, contact angles and adsorption energies at the liquid-liquid interface [15]. To achieve a thorough understanding of the emulsification process, the impact of the nanoparticles on rheology and interfacial tension is investigated since these are crucial parameters for dispersion and coalescence. Furthermore, drop size distribution characteristics are analyzed as a function of agitation speed, particle type and particle mass fraction in w/o and o/w emulsions. In future studies, these results can be used to adapt existing drop size distribution models for liquid-liquid systems to the case of nanoparticle-stabilized dispersions.

Susanne Röhl, Dr.-Ing. Lena Hohl, Maresa Kempin, Frauke Enders, Nico Jurtz, Prof. Dr.-Ing. Matthias Kraume
s.roehl@tu-berlin.de
Technische Universität Berlin, Chair of Chemical and Process Engineering, Ackerstraße 76, 13355 Berlin, Germany.

2 State of the Art

In this section, the current state of the art concerning rheology of nanoparticle suspensions, interfacial phenomena and drop size distributions is summarized.

2.1 Rheological Properties of Silica Nanoparticle Suspensions

Dispersion, coalescence and the resulting drop size distribution depend on parameters such as density, interfacial tension and the viscosity of the dispersed and continuous phase. The presence of nanoparticles in a liquid phase can lead to complex rheological behavior, especially if the nanoparticles possess an irregular shape. Nanoparticle suspensions are often shear thinning with viscoelastic properties [16–18]. The flow curves and the viscoelastic response depend on the chemical and morphological structure of the nanoparticles and their interaction with the liquid phase. Different types of interactions (particle-particle or particle-liquid) are dominant and can provoke agglomeration processes [19]. The viscosity of the oil-nanoparticle suspensions depends considerably on the nanoparticles silanol content [20]. Strong hydrogen bonds exist between the silanol groups of particles, whereas the interaction of silanol groups with weakly hydrogen-bonding liquids is less pronounced [21]. Hence, particle-particle interactions are dominant in comparison to particle-liquid interactions, especially in case of particles with high silanol content dispersed in a nonpolar phase.

Viscoelastic fluids exhibit elastic and viscous characteristics. Gel-like viscoelastic behavior with a loss factor of $tan\,\delta = G''/G' < 1$ often occurs in Pickering emulsions (storage modulus $G' >$ loss modulus G''). Particles with a lower residual silanol content (25 % SiOH) develop less or smaller agglomerates, which seem to be distributed more evenly in the organic phase in comparison to more hydrophilic particles (50 % SiOH) [20]. Furthermore, nanoparticle suspensions often show a yield stress, which is defined as the stress that must be applied to the sample before it begins to flow. Below this critical value, the sample deforms elastically, and Hooke's law is valid. The elastic flow is a reversible process and governed by the interaction of the dispersed phase and the particles. The reasons for the appearance of a yield stress are intermolecular physical interactions with bond energies below 20 kJ mol^{-1} [22]. Knowledge of the shear thinning behavior, viscoelastic properties and yield stress of the systems is crucial since it affects the fluid dynamics in different parts of the intended process, such as pumping, emulsification and separation [12, 23].

2.2 Adsorption of Nanoparticles at the Liquid-Liquid Interface

The stabilizing effect of nanoparticles in dispersions is caused by their high adsorption energy at the liquid-liquid interface, as compiled by Bresme and Oettel [24]. Their survey includes the adsorption of nanoparticles in terms of stability, self-assembly and mutual interactions of nanoparticles at the liquid-liquid interface [24]. For a single spherical particle, which is small enough that a deformation of the interface due to gravity can be neglected, an equation to calculate the energy of particle detachment from the interface can be derived. Therefore, the free energy of the system in two different states needs to be taken into account (see Fig. 1): a) the equilibrium position of a particle at the interface and b) the state when the particle is completely immersed in either the aqueous or the organic phase.

The adsorption energy for spherical particles depends on the particle radius R, the contact angle θ measured in the aqueous phase and the liquid-liquid interfacial tension $\sigma_{o,w}$ [9]:

$$E_{ads} = \pi R^2 \sigma_{o,w} (1 \pm cos\theta)^2 \quad (1)$$

The term within the brackets becomes negative if the particle is moved from the interface into the aqueous phase and positive if it is moved into the organic phase [9]. Hydrophilic silica particles lead to low contact angles ($\theta < 90°$) and promote the formation of o/w emulsions, whereas hydrophobic particles lead to high contact angles ($\theta > 90°$) and promote the formation of w/o emulsions [15, 25]. Usually the particles are dispersed in the liquid with higher wettability and this liquid becomes the continuous phase, which is in accordance with the Bancroft rule [26]. Most stable emulsions are formed using partially hydrophobic silica particles that have contact angles close to 90° and can stabilize both o/w and w/o emulsions [5, 27].

For nonspherical particles with irregular shape, the determination of a contact angle at the liquid-liquid interface is

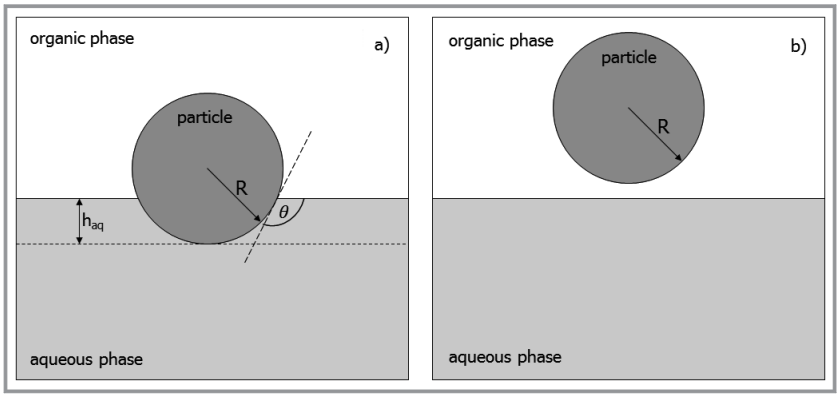

Figure 1. Spherical solid particle a) attached to the oil-water interface with immersion depth h_{aq} and contact angle θ and b) completely detached into the organic phase (according to [9]).

difficult due to the different possible particle orientations. Therefore, the description of their adsorption behavior and the determination of the adsorption energy is challenging. The influence of particle geometry on the adsorption was investigated amongst others by Faraudo and Bresme [28] who investigated prolate and oblate particles with parallel or perpendicular orientation with respect to the interface plane. They found that nonspherical particles do not adsorb at the interface if their aspect ratio β is larger than a critical aspect ratio β_c. Line tension and particle orientation also play a major role in terms of stability of nonspherical particles at the interface. The adsorption process and the energy needed to remove the particles from the liquid-liquid interface depend on particle wettability and directly influence the coalescence behavior and the drop size distributions of the systems. The particle size is another parameter influencing the drop size distribution. Tsabet et al. [13] investigated the impact of spherical glass beads with different size but identical contact angle on the drop size distribution in an agitated liquid-liquid system. With increasing particle size higher Sauter mean diameter occurred. A larger particle size influences the particle-drop collision force and the film drainage process. Additionally, the degree of interface coverage decreases, the wetted depth of the particle at the interface rises and higher adsorption times occur [13].

2.3 Drop Size Distribution in Agitated Liquid-Liquid Systems

The breakage and coalescence phenomena in stirred liquid-liquid systems and the resulting drop size distribution are defined by parameters such as tank and stirrer geometry, agitation speed (energy dissipation rate) and the physical properties such as viscosity, density and interfacial tension. For common liquid-liquid systems, various approaches to predict mean drop diameters or the whole drop size distributions can be found in literature. Semi empirical equations with the dimensionless Weber number can estimate the Sauter mean diameter in breakage-dominated systems and are often based on the correlation by Hinze [29] with $d_{32} \sim We^{-0.6}$. Coulaloglou and Tavlarides [30] published a modified empirical correlation for the Sauter mean diameter calculation in Newtonian fluids which also takes the volume fraction of the dispersed phase into account. Calabrese et al. [31] modified the Weber correlation by the viscosity vessel number, which also considers the viscosity of the dispersed phase for Newtonian fluids.

A more elaborate approach to predict drop size distributions are population balance equations (PBEs), which are often coupled with computational fluid dynamics (CFD) to account for the local fluid dynamics. They allow describing systems where coalescence cannot be neglected and include equations for the drop breakage rate, drop-drop collision frequency and drop coalescence efficiency, the number of daughter drops per breakage event and the daughter drop size distribution [30, 32, 33]. However, most PBE models assume deformable droplets with mobile interfaces, which is often not the case in presence of additives and especially in presence of solid nanoparticles [8]. So far, the accurate description of drop size distributions in presence of additives still is a challenging task and various submodels have been developed in order to describe, e.g., the effect of pH, ions or surfactants [34–36]. In contrast to surfactants, no appreciable reduction of the interfacial tension in presence of nanoparticles occurs, although this also depends on the nanoparticle type and modification [37–39]. Often the changes in physical properties such as density, interfacial tension and viscosity do not suffice to adequately predict the system behavior, so that empirical parameters need to be fitted to a given material system.

The stabilization of droplets by nanoparticles is described with two different criteria in literature: A thermodynamic approach considering that stability is achieved when the system reaches its minimal free energy, or a mechanical approach considering that stability is reached when the sum of forces is zero [13]. During the emulsification process, droplet breakage, particle/droplet approach, particle adsorption and a particle network formation leading to droplet stabilization has to occur [13]. Hence, the contact angle respectively the hydrophobicity of the nanoparticles [20] and the surface coverage respectively the nanoparticle concentration [8] possess an influence on the drop size distributions. Due to the rheological properties particularly at high nanoparticle mass fractions and the steric barrier caused by the presence of nanoparticles at the interface [8, 13], an impact on drop deformation, drainage time and film rupture during coalescence occurs.

The effects of formulation on the final emulsion properties produced with a high energy input by ultrasonication were already investigated by numerous authors [4, 10, 12, 20, 23, 27, 40, 40, 41]. These emulsions often are stable towards coalescence over a long period due to droplet sizes in the range of a few micrometers. A rising nanoparticle content leads to smaller drop sizes until a constant value is reached and the interface of all generated droplets can be completely covered with particles.

The influence of the energy input is amongst others investigated by Skale et al. [42] who compared the dispersion devices ultrasonication and ultraturrax. However, there still is a lack of studies investigating the energy input. The final drop size distribution is governed by two effects: If enough particles are available to cover the complete interfacial area, the final drop size distribution is determined by the interface generation capacity of the dispersion device. If the particle concentration does not suffice to cover the complete interface, coalescence occurs until the interface is completely covered and the final drop size distribution is governed by the coverage capacity [13]. However, the dispersion and coalescence mechanisms are barely understood [13]. Previous studies that considered this often focused on characteristic diameters rather than the com-

plete drop size distribution. The work by Tsabet and Fradette [13] is one of the few examples where energy input induced by stirring was used in order to achieve a fundamental understanding of the emulsification mechanisms itself. A comparison of o/w emulsions in an agitated tank stabilized with regular and modified glass particles showed that droplet stabilization is highly sensitive to the viscosity of the dispersed organic phase, particle size and particle wettability. High oil/particle affinity led to emulsions with the smallest drop sizes and a narrow drop size distribution [13].

The sedimentation of droplet swarms is extremely sensitive to droplet size, dispersed phase fraction and rheology [43]. Furthermore drop-drop and drop-interface coalescence rates in concentrated emulsions are important parameters for the long-term emulsion stability [36, 43, 44], which can be analyzed by observing the sedimentation and the height of the completely coalesced interface over time with an external camera. If the sedimentation speed exceeds the coalescence, a dense-packed zone is formed where droplets deform and grow in size until they coalesce with the interface. In case of very low coalescence rates, other effects such as Ostwald ripening in the dense-packed zone can become relevant.

This work aims to analyze the dispersion and coalescence mechanisms with a detailed drop size distribution analysis in stirred tanks. The complex rheological behavior and the impact of nanoparticles with different characteristics at the interface are effects that need to be considered in future modeling approaches. Thereby, the stirred systems possess a significantly lower energy input compared to the systems dispersed via ultrasonication, so that not only the final emulsion characteristics are quantified. The impact of silica particles with different BET values and hydrophobicity on physical properties, dispersion and coalescence was quantified. The influence of nanoparticles on the coalescence behavior is also investigated with batch settling experiments by optical evaluation of the dynamic phase separation process [44].

3 Materials and Methods

The used substances were *n*-heptane (Merck, purity $\geq$ 99 %), ultrapure water (κ = 0.055 S cm^{-1}, Purelab flex 2, Elga) and different silica particles. The composition of the systems is described using the oil mass fraction α, the mass fraction of particles w_p in relation to the mass of dispersed phase and the mass fraction of particles $w_{p,s}$ in a suspension:

$$\alpha = \frac{m_{n-heptane}}{m_{n-heptane} + m_{water}} \quad (2)$$

$$w_p = \frac{m_{particles}}{m_{dispersed\ phase} + m_{particles}} \quad (3)$$

$$w_{p,s} = \frac{m_{particles}}{m_{n-heptan} + m_{particles}} \quad (4)$$

3.1 Properties of Silica Nanoparticle

Fumed silica particles with different hydrophobicity and a fractal-like, irregular shape (Wacker Chemie AG) were used, which were manufactured by flame pyrolysis and hydrophobized with dichlorodimethylsilane to two extents (50 % SiOH and 25 % SiOH). The particles possess moreover different specific surface areas (BET values) as summarized in Tab. 1. They were used without additional chemical modification. The fused aggregates of primary particles possess an average size of F_v = 150 nm and F_h = 50 nm [8]. The irregular shape of the particles is clearly visible in scanning electron microsopy (SEM) images, as depicted for example in [12, 20].

Table 1. Properties of the silicia nanoparticles according to manufacturer specifications.

Name	SiOH content [%]	specific particle surface (BET) [m^{2}g^{-1}]
HDK H20	50	200 ± 30
HDK H18	25	200 ± 30
HDK H30	50	250 ± 30

The adsorption energies of the particles (Eq. (1)) were calculated with the interfacial tension $\sigma_{o,w}$ = 52.0 ± 0.3 mN m^{-1} measured by pendant drop method at T = 293 K (cf. Sect. 3.4). Due to their different residual silanol content H20 and H30 particles might have a lower contact angle closer to 90° in comparison to the more hydrophobic particles H18 with contact angles greater 90°. The impact of the size on the adsorption energy is exemplary calculated for two different radii and two contact angles, which represents the relevant range in this work. For a constant particle size, the more hydrophobic particles (H18) will not adhere to the interface as strongly as H20 and H30 due to their higher contact angle that reduces the adsorption energy (cf. Tab. 2). The calculation is a rough estimation, since the specific particle surface area and different possible particle orientations at the interface due to the particle polydispersity were disregarded.

Table 2. Calculated adsorption energy for particles at the water/*n*-heptane interface at T = 293 K for $\sigma_{o,w}$ = 52.0 ± 0.3 mN m^{-1} with variation of contact angle and size.

Particles radius r_p [nm]	Contact angle θ_{ow} [°]	Adsorption energy E_{ads} [kT]
50	90	1986
100	90	3972
100	120	993

A variation in specific surface area can influence the size and spatial complexity of the particles. Hence, the BET value might influence the attachment and interlocking of

particles at the interface, which can result in different contact angles and adsorption energies. Consequently, the drop sizes in emulsions may differ for varying BET values.

3.2 Density of Pure Components and Suspensions

The density of the pure components according to manufacturer specifications and literature are ρ(*n*–heptane) = 683 kg m^{-3}, ρ(water) = 998.20 kg m^{-3} and ρ(particles) = 2200 kg m^{-3} at T = 293 K. The densities of the *n*-heptane/ nanoparticle suspensions are summarized in Tab. 3 as a function of particle mass fraction. They were calculated using the respective particle mass fractions while neglecting possible excess volume. Since the different silica particle types possess the same density, no differences between HDK H18, H20 and H30 suspensions occur.

Table 3. Calculated densities of the *n*-heptane/silica nanoparticle suspensions (T = 293 K).

$w_{p,s}$ [wt %]	Density ρ [kg m^{-3}]
0.05	683.24
0.15	683.71
0.25	684.18
0.5	685.36
0.75	685.55
1	687.74
2	692.55

For rheological and interfacial tension measurements the particles were dispersed in *n*-heptane with an ultrasonication homogenizer (Bandelin Sonopulus HD70, P = 70 W, f = 20 kHz, 75 % amplitude) for 5 min. The sample volume was V = 0.05 L per batch. The second liquid phase for the interfacial tension and drop size measurements was ultrapure water. For the drop size measurements in agitated systems, nanoparticles were added to the tank without previous suspension to avoid the use of additional dispersion devices. No remarkable change in drop size distribution was observed while comparing the addition of nanoparticles with or without previous suspension.

3.3 Suspension Rheology

Rheological measurements were conducted using a tempered cone and plate geometry (Anton Paar MCR 302, Measurement system CP60-1: cone diameter 59.978 mm, angle 1.008°, gap size 0.117 µm). All measurements were performed at T = 293 ± 0.1 K. The independence of the results from the measurement time per data point was checked in order to exclude an influence on the flow curves and oscillatory measurements. Shear rate, shear stress, deformation and angular frequency were increased in logarithmic scale. Before each experiment, the samples were freshly produced by ultrasonication and rested on the plate until a normal force of F_N = 0 N was achieved. The yield stress was determined experimentally in this work to avoid approximation errors due to the choice of regression models, analysis area and shape of the curve.

3.4 Interfacial Tension

The liquid-liquid interfacial tensions were measured via pendant drop method (Dataphysics OCA15). To verify the purity of all device components, the interfacial tension of pure *n*-heptane against water ($\sigma_{o,w}$ = 52.0 ± 0.3 mN m^{-1} at T = 293 K) was checked against literature values ($\sigma_{o,w}$ = 51.24 mN m^{-1} [45]) before each measurement. A droplet of *n*-heptane/ nanoparticle suspensions was created at the tip of a bent nozzle pending in water. The drop volume was maintained as high as possible (> 15 µL) to minimize errors during the optical evaluation method. The measurements were carried out in a tempered measuring cell at T = 293 ± 0.1 K. Steady-state values were taken after the interfacial tension reached a constant value and at least three replicate measurements were carried out.

3.5 Agitated Tank

Drop size measurements were performed in a temperature-controlled agitated tank at T = 293 ± 0.1 K (cf. Fig. 2a). The total volume was kept constant at V = 700 mL. The tank dimensions were D = 0.1 m, H/D = 1.6, h_b/D = 1.7, d_{st}/D = 0.45, and h_{st}/D = 0.45. A Rushton turbine (h_{st} = 0.045 m, d_{st} = 0.045 m, blade height h_{sb} = 0.006 m, width w_{sb} = 0.01 m, thickness s_{sb} = 0.001 m) and four rectangular baffles (height h_b = 0.12 m, width w_b = 0.07 m, thickness s_b = 0.001 m) were used. Stirrer speeds of n = 700, 800 and 900 rpm were investigated, which correspond to energy dissipation rates determined by using torque measurements in the range of $\varepsilon \approx$ 0.9–2.1 W kg^{-1}. Drop sizes were measured in situ with an endoscope technique (Sopat GmbH) connected to a camera (GX 2750, Allied Visions Technology). Two different endoscopes with transflexion principle were used with a measurement range of particle diameters between 8–600 µm and 25–1000 µm. The endoscope was positioned at stirrer height in a horizontal distance of 0.01 m to the stirrer. To improve image quality, a mirror was attached to the tip of the endoscope with a gap size of 0.006 m. Image analysis was carried out with an algorithm for automated drop detection (Sopat GmbH).

The shear rate distribution inside the tank was estimated with computational fluid dynamics using the commercial software StarCCM+. The simulations were performed under steady-state conditions using a moving reference

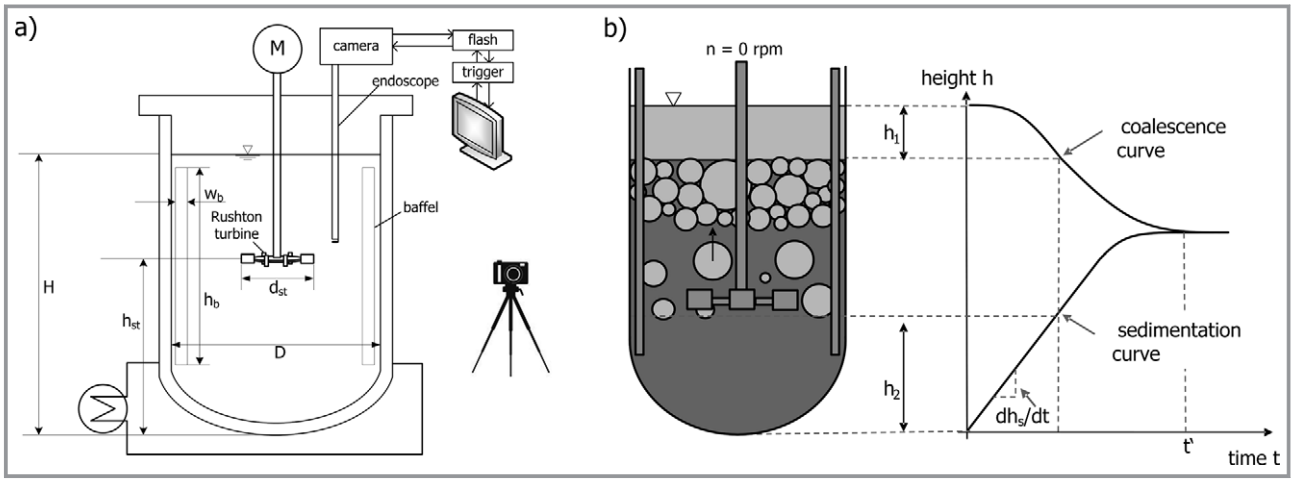

Figure 2. a) Experimental setup with endoscope technique and external camera, b) scheme of batch settling experiments (according to [44]).

frame with the realizable k-ε turbulence model. A polyhedral mesh was used, and the emulsion was approximated as a homogeneous mixture with a specified mixture density and a shear rate dependent viscosity, by fitting experimental flow curves with the Carreau model. The magnitude of the symmetric velocity gradient tensor was used as a measure for the shear rate, as proposed by Wollny [47]. The representative shear rate near the stirrer was evaluated in a cylindrical element with the dimensions h_{crit} = 0.023 m and r_{crit} = 0.025 m around the stirrer. The shear rates in the bulk phase were evaluated in the circulating zones of the tank outside the specified stirrer range.

Batch settling experiments were carried out in the same vessel to achieve additional information on the coalescence behavior by determination of sedimentation velocity and separation time (Fig. 2a). Pictures were taken in defined time steps after agitation stop with an external single lens reflex camera (Canon EOS 700 D). The coalescence curve signifies the height of the completely coalesced interface, as shown schematically in Fig. 2b). The slope of the sedimentation curve can be used to estimate the sedimentation velocity $v_s = dh_s/dt$ of the droplet swarm assuming that no coalescence occurs during free sedimentation [44]. The sedimentation velocity can also be calculated with a swarm sedimentation model based on the drop size measurements and vice versa [44, 46].

4 Results and Discussion

The results concerning suspension rheology, interfacial tension and drop size distribution characteristics are provided in the following.

4.1 Suspension Rheology

Pure *n*-heptane and water possess Newtonian rheological behavior. The three investigated nanoparticle types are partly hydrophobic and can only be suspended in the organic phase. For the following rheological analysis, three replicate measurements of the suspensions were performed. To improve graph clarity, the results are shown as arithmetic mean values without error bars. The maximal relative error of the dynamic viscosity calculated by the standard deviation of three replicate measurements was ±15 % for low shear rates ($\dot{\gamma}$ = 1–10 s^{-1}) and 9 % for higher shear rates ($\dot{\gamma}$ = 10 – 1000 s^{-1}). The deformation at given shear stress within the elastic region had a maximal relative error of ±22 %.

All investigated nanoparticle suspensions show shear thinning flow behavior. With increasing particle mass fraction, the flow curves are shifted towards higher viscosities, as is exemplary shown for HDK H20 particles in Fig. 3a.

The suspended particles formed particle-particle agglomerate network structures due to their fractal and irregular shape, which break up with increasing shear rate [20]. Agglomerates could also be formed due to hydrogen bonding between particles and *n*-heptane. In comparison to a more hydrophobic solvent (e.g., 1-dodecene) [20], the flow curves with *n*-heptane were shifted towards higher viscosities, caused by a higher hydrogen bonding ability of *n*-heptane in comparison to 1-dodecene. For $w_{p,s}$ = 0.5–2 wt % the systems exhibited a region with dilatant flow that led to a local maximum of dynamic viscosity. It became more pronounced with increasing particle mass fractions. This could be caused by a reorientation and accumulation of the particles at shear rates between $\dot{\gamma}$ = 20–50 s^{-1}. In stirred tanks, a broad range of shear rates can occur due to local fluid dynamics and internals (e.g., distance to the stirrer) so that the dependency of dynamic viscosity on shear rate and its effect on drop breakage and coalescence phenomena should

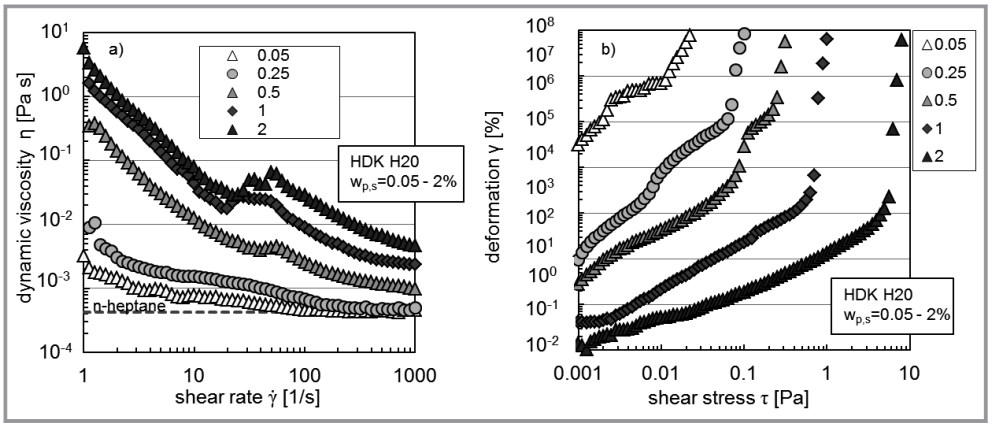

Figure 3. Suspension rheology of HDK H20 particles in *n*-heptane with different HDK H20 particle mass fractions. a) Dynamic viscosity as a function of shear rate, b) deformation as a function of shear stress.

be evaluated with care. Calabrese et al. [31] investigated the impact of the dispersed phase viscosity on drop size distributions in stirred tanks with different silicone oils of Newtonian rheology while keeping the interfacial tension and densities approximately constant. They determined an increase of Sauter mean diameter by a factor of approximately 2.3 if the dispersed phase viscosity increased from 0.1 to 0.5 Pa s. For these viscosities, the drop sizes were normally distributed, whereas they became lognormal for higher viscosities around 5 Pa s. Due to small dispersed phase fractions, the assumption of a breakage-dominated system without coalescence and spatial independence of the steady-state drop size distribution was applied. Tsabet and Fradette [13] compared different oils, which mainly varied in dynamic viscosity (η = 0.00953–4.88 Pa s) and density (ρ = 935–975 kg m^{-3}). The oils were dispersed in glass particle-water suspensions. For constant particle concentration, mixing time and stirrer speed they observed constant distribution widths (based on $d_{v,10}$, $d_{v,90}$ and d_{32}) and nearly constant diameters for oils with $\eta < 0.4855$ Pa s. In this range, the droplet size was determined by the coverage potential or the particle concentration. At higher viscosities, the entire emulsification process was influenced by the interface generation capacity (power input) and the distribution width increased.

In Fig. 3b the impact of rising particle mass fraction on the deformation over shear stress is illustrated for HDK H20 particles in *n*-heptane. The slope of the deformation changes between the linear-elastic and viscous deformation regime mostly with a sharp bend [22]. The change in slope determines the yield stress that needs to be applied before the samples begins to flow. The first change of slope in the systems presented here is shifted towards higher values with increasing particle mass fraction and an increase over two decades from τ_0 = 0.01 Pa ($w_{p,s}$ = 0.05 wt %) to τ_0 = 5 Pa ($w_{p,s}$ = 2 wt %) arises. Hence, the shear modulus $G = \tau/\gamma$ rose in the elastic region with increasing particle concentration. This trend is in accordance with literature [16, 48]. A yield transition range instead of a sharp yield point occurred for suspensions with low particle mass fractions ($w_{p,s}$ = 0.05 wt % and $w_{p,s}$ = 0.25 wt %). It has to be considered that the determined yield stresses depend on the measurement conditions, like the rotation speed resolution of the rheometer.

The effect of nanoparticle types with different silanol content (i.e., hydrophobicity) and different specific surface areas are illustrated in Fig. 4a using the relative viscosity. It is defined by the quotient of the dynamic suspension viscosity at a shear rate of $\dot{\gamma}$ = 100 s^{-1} and the dynamic viscosity of pure *n*-heptane:

$$\eta_r = \frac{\eta_{\dot{\gamma}=100\ 1/s}}{\eta_{n-heptane}} \tag{5}$$

With rising particle mass fraction, the increase of relative viscosity became more pronounced for H20 in comparison to H30 and H18 particles. The relative viscosity rose by a factor of 22 between $w_{p,s}$ = 0 wt % and $w_{p,s}$ = 1 wt % for H20, but only by a factor of 2.6 for H30 and H18.

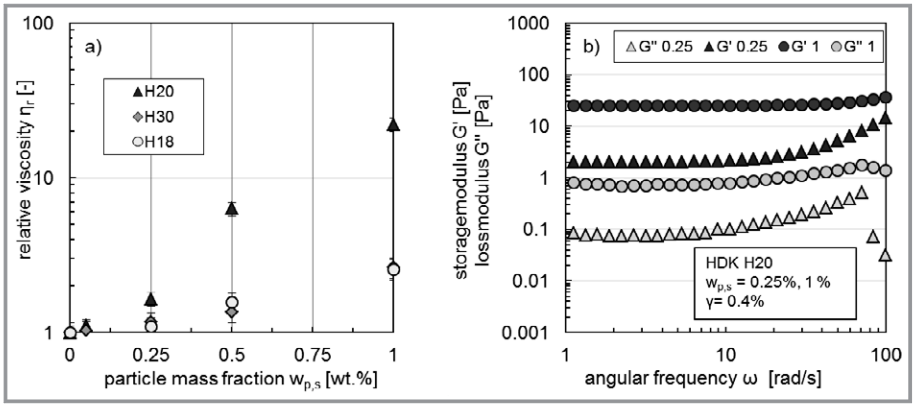

Figure 4. a) Relative dynamic viscosity as a function of particle mass fraction for HDK H20, H30 and H18 suspended in *n*-heptane, b) frequency sweep measurements of HDK H20/*n*-heptan suspensions for $w_{p,s}$ = 0.25 and 1 wt % values are illustrated for γ = 0.4 %, T = 293 K.

With CFD simulations, the volumetric mean value of the representative shear rate was calculated as described in Sect. 3.5 around the stirrer ($V_{stirrer}$) and in the bulk phase (V_{bulk}) of the reactor. The calculations are summarized in Tab. 4 and were performed for pure water and for o/w emulsions (α = 0.15) with *n*-heptane stabilized by HDK H20 particles with w_p = 0.5 wt % and w_p = 1 wt %. Agitation speeds of n = 700 rpm and n = 900 rpm were examined in steady state.

The impact of higher agitation speeds on the shear rates is clearly visible for all material systems, especially in the volume around the stirrer. For rising nanoparticle content and increased shear-thinning behavior, the shear rates in the stirrer region are barely affected. Larger differences occur in the bulk volume while comparing 0.5 wt % and 1 wt % of particles. Due to the shear-thinning rheology of the dispersed phase in the systems presented here, an estimation of the impact of the dynamic viscosities on the drop size distributions is not trivial. The drop breakage should mainly occur in regions with large shear rates ($V_{stirrer}$), where differences between particle concentrations and particle types are less pronounced and the viscosity is comparatively low (cf. Fig. 4a and Tab. 4). However, the shear rates and corresponding viscosities vary significantly between the bulk phase and the region in vicinity to the stirrer. In contrast to the aforementioned work by Calabrese et al. [31] coalescence cannot be neglected in this work due to the higher dispersed phase fractions and the dependency of coalescence on the nanoparticle mass fraction. Coalescence will mainly occur in the bulk phase, where lower shear rates or higher viscosities exist in comparison to the volume near the stirrer (cf. Tab. 4 and Fig. 3a). Higher viscosities usually hinder the coalescence probability since it influences the flow during film drainage, the drag coefficient, the relative velocity of the droplets and the velocity boundary condition of the drainage flow [36].

The nanoparticle suspensions also showed viscoelastic flow properties, which were characterized using oscillatory measurements. The linear viscoelastic (LVE) area and an appropriate deformation (γ = 0.4 %) were determined with an amplitude sweep. Frequency sweeps for two H20 particle concentrations are shown in Fig. 4b. Viscoelastic flow behavior with $G' > G''$ occurred, which corresponds to gel character of the suspensions. With higher nanoparticle content the moduli were shifted towards higher values. For low frequencies, nearly constant storage and loss moduli were observed, indicating stability of the suspensions towards sedimentation.

The rheological properties of the investigated nanoparticle suspensions are complex, which has an impact on the flow field in the tank and can have a significant influence on the drop breakage, the number of daughter droplets, the deformation and film drainage during coalescence, and the resulting droplet size distribution. In the following, the impact of nanoparticles on the interfacial tension will be discussed before the drop size distributions themselves are quantified.

4.2 Interfacial Tension

The liquid-liquid interfacial tension was measured for different nanoparticle mass fractions and all three nanoparticle types. Fig. 5a shows the equilibrium interfacial tensions for HDK H20 particles as an example. The error bars indicate an experimental error of 2 %, which was the maximum percentage deviation in three replicate measurements. The nanoparticles barely influenced the interfacial tension, since

Table 4. Volumetric mean values of calculated representative shear rates $\dot{\gamma}$ [s^{-1}] with CFD in the volume around the stirrer ($V_{stirrer}$) and in the bulk phase (V_{bulk}).

Composition	Shear rate $\dot{\gamma}$[s^{-1}]			
	n = 700 rpm, $V_{stirrer}$	n = 900 rpm, $V_{stirrer}$	n = 700 rpm, V_{bulk}	n = 900 rpm, V_{bulk}
Water	163	210	39	50
α = 0.15, w_p = 0.5 wt %	168	219	34	58
α = 0.15, w_p = 1 wt %	159	215	16	32

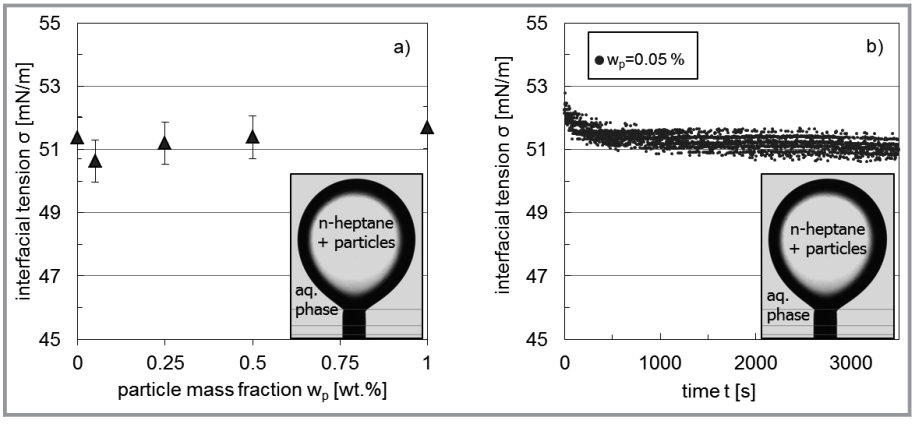

Figure 5. Liquid-liquid interfacial tension of HDK H20 suspended in *n*-heptane against water, T = 293 K a) for different particle concentrations in steady state, b) dynamic interfacial tension for w_p = 0.05 wt %.

the values fluctuate in the range of the error bars. The same result was achieved with HDK H18 and HDK H30 particles (see Tab. 5). The transient curve for a particle mass fraction of w_p = 0.05 wt % depicted in Fig. 5b shows that the measurement time was long enough to achieve a constant equilibrium interfacial tension value.

Table 5. Steady state interfacial tension σ of *n*-heptane/silica nanoparticle suspensions of HDK H18, HDK H30 and HDK H20 particles for different particle mass fractions w_p against water. The average value of three replicate measurements is in each case given with a maximum standard deviation for all measurements of ±0.6 mN m^{-1}.

w_p [wt %]	σ_{H18} [mN m^{-1}]	σ_{H30} [mN m^{-1}]	σ_{H20} [mN m^{-1}]
0.25	52.03	50.60	51.20
0.5	51.79	52.17	51.38
1	49.6	51.87	51.69

The impact of nanoparticles on the interfacial and surface tension is discussed controversially in literature. Nanoparticles adsorb at the liquid-liquid interface, but it is not clearly pointed out if a reduction of interfacial tension should occur. Constant surface and interfacial tensions were observed for example for silica particles at different pH values and particle concentrations, for hydrophobized silica nanoparticles with rising particle mass fractions up to 1 wt % at constant pH [38], or for aqueous suspensions of spherical silica nanoparticles with particle diameters in the range of 6–45 nm and particle volume fractions between 0.1–10 % [49].

Dugyala et al. [50] investigated aqueous suspensions with 1 wt % silica nanoparticle against decane and reported only a slight decrease of the interfacial tension by 0.5 mN m^{-1}. Similar results were also found in water/1-dodecene/HDK H20 systems under the condition that the oil phase does not contain any surface-active impurities [8]. These results are in agreement with the interfacial tension values shown in Fig. 5. It should be noted that different behavior can be observed for other nanoparticle types and with different particle surface modifications [51–53]. A review concerning the impact of nanoparticles on interfacial tension is provided by Fan and Striolo [39].

An alternative to interfacial tension measurements via pendant drop method is to determine the surface pressure with a Langmuir trough. The surface pressure π during compression of a particle monolayer per definition describes the difference between the surface tension of the pure liquid and the surface tension of the liquid phase with particles [54]. Horozov et al. [55] reported different increases in surface pressure while comparing HDK H20 (π = 45 mN m^{-1}) and H18 (π = 30 mN m^{-1}) particles. This impact on surface pressure and the corresponding change in interfacial tension are not in agreement with the pendant drop results. The main reason for this behavior could be different degrees of interface coverage during pendant drop and surface pressure measurements.

4.3 Drop Size Distributions

The drop size distributions were investigated as a function of particle mass fraction in o/w and w/o emulsions with different particle types. Furthermore, an analysis of distribution self-similarity is performed, and the coalescence behavior is determined after abrupt changes in agitation speed.

4.3.1 Influence of Particle Concentration in o/w and w/o Emulsions

With a variation of the dispersed phase fraction induced by a different oil/water ratio α, the systems with HDK H20 particles could be forced to develop o/w emulsions (α = 0.15) or w/o emulsions (α = 0.85). This inversion affected the drop breakage and coalescence phenomena and the drop size distribution of the systems. Steady-state values for o/w and w/o emulsions using different HDK H20 particle mass fractions at a constant stirrer speed of 900 rpm are depicted in Fig. 6a. The error for all endoscope

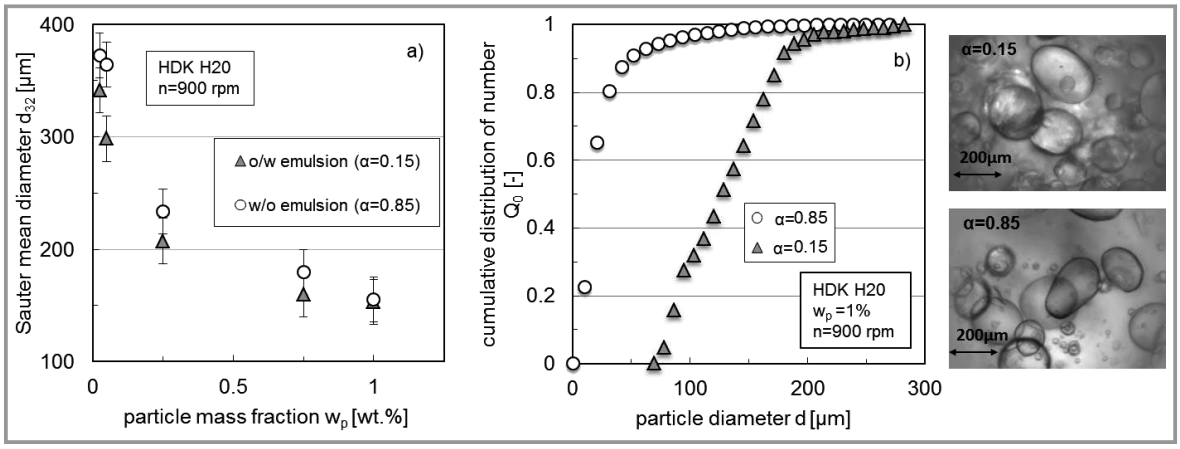

Figure 6. Steady-state values for agitated o/w and w/o emulsions with HDK H20 particles, n = 900 rpm, T = 293 K. a) Sauter mean diameter over particle mass fraction, b) drop size distributions for a constant particle mass fraction of w_p = 1 wt %.

measurements is assumed to be ±20 µm while also considering the error due to the automated drop detection [56].

With increasing particle mass fraction, the Sauter mean diameters of both emulsion types decreased, which is in accordance with literature [4, 10, 13]. The higher number of particles led to rising interface coverage so that coalescence was more effectively hindered and smaller droplets occurred.

The general shape of the curves is in accordance with the ones described by Chevalier [41]. Larger Sauter mean diameters occurred in w/o emulsions for low particle mass fractions. This difference reduced with rising particle content until nearly the same Sauter mean diameters existed at a particle mass fraction of w_p = 1 %. The corresponding cumulative distributions of number Q_0 for w_p = 1 % are shown in Fig. 6b and characteristic diameters are summarized in Tab. 6. A comparison of the minimum and maximum diameters d_{min} and d_{max} and the number- and volume-based spans ($span_0$, $span_3$) clearly indicates differences in the distribution widths. The drop size distribution of the w/o emulsion (α = 0.85) in Fig. 6b had a smaller minimum and larger maximum diameter and the complete distribution spanned a wider droplet size range in comparison to α = 0.15. Hence, the similar Sauter mean diameters were mainly a coincidence and do not allow drawing detailed conclusions for the actual drop size distributions in o/w and w/o emulsions.

Table 6. Comparison of characteristic diameters and normalized drop size distribution widths of w/o and o/w emulsions stabilized with HDK H20 particles w_p =1 wt %.

Parameter	α	
	0.15 (o/w)	0.85 (w/o)
d_{32} [µm]	156	153
d_{min} [µm]	69	16
d_{max} [µm]	282	404
$span_0$, $d_{n,90}$–$d_{n,10}/d_{n,50}$ [–]	0.74	2.23
$span_3$, $d_{v,90}$–$d_{v,10}/d_{v,50}$ [–]	0.92	1.17

In both systems, nonspherical droplets were observed (cf. Fig. 6, right). At high particle concentrations, the surface coverage of the particles is so high that the nanoparticles interlock and arrested coalescence occurs. Due to the resulting stiffness of the liquid-liquid interface, the deformed droplets are not able to return into their energetically preferred spherical shape and remain trapped in an intermediate stage of coalescence [3, 57]. The combined surface area of the deformed droplets is higher than the interfacial area of spherical droplets. With the applied drop detection algorithm, only spherical droplets could be determined. To quantify how the arrested coalescence affected the automated drop detection results and the drop size distributions, a manual drop detection of nonspherical droplets was performed using the software ImageJ. To reduce the expenditure of time, only the experiment with the highest amount of nonspherical droplets (α = 0.85, HDK H20, w_p = 1 %, n = 900 rpm, 300 images) was analyzed. In the investigated image series, 2.87 % of all droplets possessed a nonspherical shape. The circular equivalent diameter $d_{A,i}$ is used to determine the Sauter mean diameter d_{32}.

Including the nonspherical droplets into the image analysis increased the Sauter mean diameter by 10 µm, i.e., by 6 %. Although the image analysis clearly is flawed when it comes to nonspherical droplets, these errors were still in the range of expected deviations and not the reason for the observed distribution shapes shown in Fig. 6b.

4.3.2 Self-Similarity

The comparison between o/w and w/o distributions in Fig. 6 b showed an immense impact of the dispersion type on the distribution shape. Therefore, the self-similarity was investigated also for other process parameters. The number-based standard deviations σ_n normalized with the Sauter mean diameter d_{32} are shown in Fig. 7 for different agitation speeds, particle mass fractions and both o/w and w/o emulsions. Kraume et al. [58] showed that normalized standard deviations in stirred tanks with water/oil systems often lead to constant values of $\sigma_n/d_{32} \approx 0.32 \pm 10$ %. A change of coalescence behavior, induced for example by ions or a change of pH, can reduce this value [58]. In w/o systems with amphiphilic molecules a value of $\sigma_n/d_{32} \approx 0.35$ was found while varying agitation speed, temperature and tank geometry [59]. In case of the nanoparticle-stabilized dispersions presented here, the values deviate around an arithmetic mean of $\sigma_n/d_{32} \approx 0.32$. Thereby, the values of o/w emulsions (filled symbols) show fewer fluctuations than the values of the w/o emulsions (blank symbols). No clear impact of the increasing nanoparticle concentration and corresponding reduced coalescence behavior on the σ_n/d_{32} values was observed in these systems.

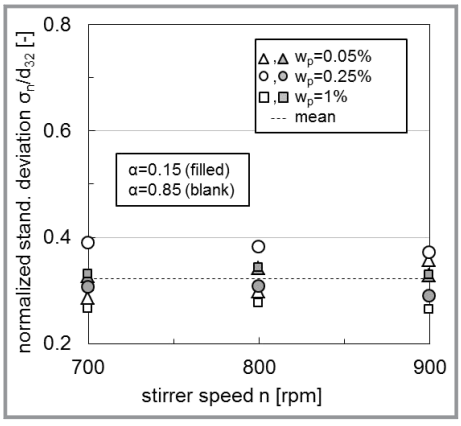

Figure 7. Normalized number-based standard deviation σ_n/d_{32} of HDK H20 emulsions in steady state for different agitation speeds and particle mass fractions (filled symbols α = 0.15, blank symbols α = 0.85) at T = 293 K.

Fig. 8 shows number-based distributions Q_0 and volume-based distributions Q_3 for all process conditions with the exception of the already discussed o/w and w/o comparison. The drop size d on the abscissa was normalized either with the Sauter mean diameter or with the arithmetic mean diameter. All distributions nearly collapse onto each other, which indicates self-similarity despite variations of stirrer speed and nanoparticle concentration for a constant $\alpha = 0.15$.

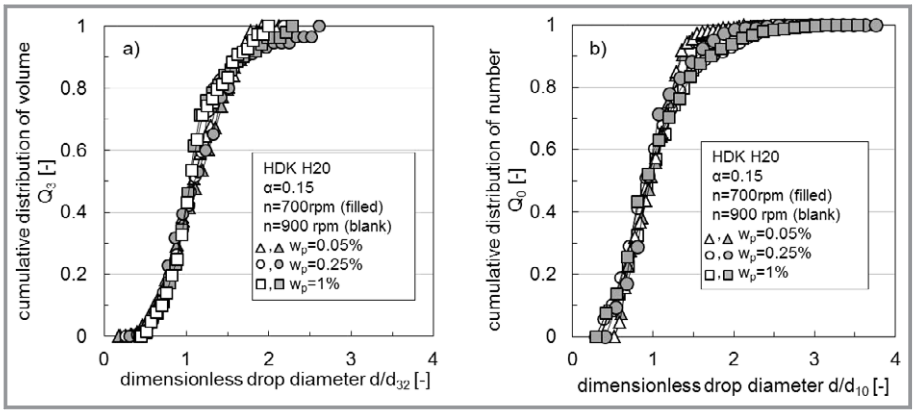

Figure 8. Cumulative drop size distribution of HDK H20 emulsions with $\alpha = 0.15$ in steady state of a) volume Q_3 and b) number Q_0 over the dimensionless drop diameter d/d_{32} or d/d_{10}, respectively. Particle mass fraction and stirrer speed were varied, $T = 293$ K.

4.3.3 Influence of Nanoparticle Type

In Figs. 9a and 9b the Sauter mean diameter and cumulative distributions of number of o/w emulsions with HDK H20 particles are compared to HDK H30 particles. The steady-state Sauter mean diameters indicate that the higher specific surface area of the HDK H30 particles led to larger Sauter mean diameters for all particle concentrations. The same holds true for the drop size distributions, since the HDK H30 particles led to larger droplets especially above the 80 % percentile (see Fig. 9b). Though the wettability of the particles is equal, the coalescence was stronger inhibited by particles with a lower specific surface area. If with increasing BET value the fractal structure of the particles rises, one particle can cover a larger interfacial area. However, this is not in accordance with the lower drop sizes at lower BET values observed here. The higher specific surface area might influence the contact angle and, therefore, the attachment and collision of the particles at the interface.

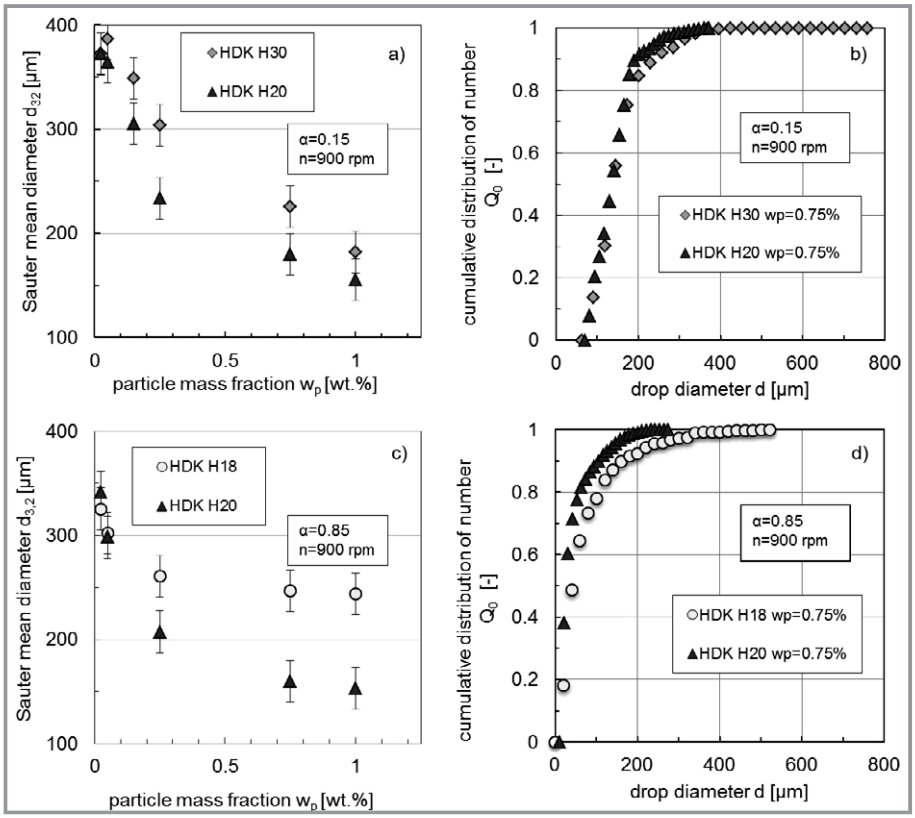

Figure 9. a) Steady-state Sauter mean diameter with different particle concentrations for HDK H20 and HDK H30, $\alpha = 0.15$, $n = 900$ rpm, b) cumulative drop size distribution of number for $w_p = 0.75$ wt % for HDK H20 and HDK H30 emulsions, $\alpha = 0.15$, $n = 900$ rpm, c) steady-state Sauter mean diameter with different particle concentrations for HDK H20 and HDK H18, $\alpha = 0.85$, $n = 900$ rpm, d) cumulative drop size distribution of number for $w_p = 0.75$ % for HDK H20 and HDK H18 emulsions, $\alpha = 0.85$, $n = 900$ rpm and $T = 293$ K. A comparison of particles with different silanol content is performed in Fig. 9c and 9d.

Highly irregular shaped and larger particles might also have a positive effect on the film drainage during coalescence. At the highest particle mass fraction, the Sauter mean diameters still decline but already nonspherical droplets occurred for HDK H30 and HDK H20 at $w_p = 1$ wt %. This leads to the conclusion that the interface was already completely occupied with nanoparticles at $w_p = 1$ wt % and no further decline of droplet size with rising particle mass fraction would occur.

The higher silanol content of 50 % of HDK H20 particles led to smaller Sauter mean diameters in comparison to

HDK H18 with 25 % silanol content. The corresponding H20 distribution of number Q_0 shown in Fig. 9d is shifted towards smaller droplet sizes. The SiOH content led to different contact angles (cf. Tab. 2) and the result is in agreement with the estimated lower adsorption energy for the more hydrophobic particles HDK H18 in comparison to HDK H20. The intermediate hydrophobicity of HDK H20 induced a higher interface coverage rate of nanoparticles and a better coalescence hindrance of the droplets at all mass fractions. The appearance of nonspherical droplets in HDK H20 emulsions at w_p = 0.75 % and w_p = 1 % supports this argument. No nonspherical droplets and, hence, no arrested coalescence was observed for HDK H18 emulsions. Consequently, not all particles of HDK H18 adsorbed at the interface.

Binks and Lumsdon [60] analyzed water-toluene w/o emulsions with spherical silica particles and toluene volume fractions of 0.5 prepared by ultrasonication. In agreement with our results, the volume distribution for particles with 50 % SiOH content was shifted to lower drop diameters in comparison to particles with 20 % SiOH [60]. Furthermore, the emulsions with 50 % SiOH exhibited a bimodal distribution of volume, which was not the case for 20 % SiOH. In contrast to Binks and Lumsdon no bimodal drop size distribution occurred for particles with 50 % SiOH content (cf. Fig. 9d) in this work, which could be caused by the different power inputs, particle geometries or dispersed phase volume fractions.

4.3.4 Impact of Nanoparticles on Coalescence Behavior

The impact of nanoparticles on the coalescence behavior was analyzed by abruptly changing the energy input in the agitated system from n = 900 to 700 rpm after reaching steady-state conditions. The response in terms of droplet sizes is depicted in Fig. 10a for different particle concentrations. The coalescence was severely hindered so that the steady-state drop diameters reduced with rising particle concentration. After reaching a critical surface coverage around w_p = 1 %, the oil-water interface was nearly fully coated with particles so that coalescence was inhibited, and a reduction of energy input did not lead to an increase of the Sauter mean diameter within the considered time frame.

Fig. 10b shows the response for different number-based mean diameters for a particle concentration of w_p = 0.25 %. It is known that the coalescence efficiency is a function of drop size, although various partly contradictory descriptions of this relation can be found in literature [32]. For example, a rising coalescence efficiency, a curve with a maximum or a declining coalescence efficiency with rising droplet sizes were reported [32]. The mechanisms are often divided into different cases such as coalescence of a) nondeformable rigid droplets, b) deformable droplets with immobile interfaces or c) deformable droplets with (partly) mobile interfaces [32]. In nanoparticle-stabilized emulsions, the droplet ability to deform and the interface mobility depend on the interface coverage with nanoparticles. The value of $d_{n,10}$ indicates that 10 % of all droplets possessed diameters $\leq$ 100 µm. The change in energy input did not affect this value, leading to the conclusion that the smallest fraction of droplets is stabilized against coalescence because their surface area was nearly fully covered by nanoparticles. For comparison, a clear impact of the agitation speed on the 90 % percentile value $d_{n,90}$ was observed in Fig. 10 since an increase of $\Delta d_{n,90}$ = 50µm occurred after the step-wise reduction of agitation rate. Consequently, the larger droplets exhibited a different coalescence behavior, caused by their size and their lower degree of interface coverage. Hence, the choice of a coalescence model in partly nanoparticle-stabilized emulsions is not a trivial task.

The coalescence behavior was also analyzed for HDK H20 stabilized o/w emulsions using phase separation experiments, where the agitation speed was abruptly changed to 0 rpm and the dynamic separation behavior was determined with an external camera. The lack of droplet movement relative to the endoscope after agitation stop prevented a representative drop size quantification. Fig. 11a shows the dynamic phase separation process over time. The lower curves represent the sedimentation of the organic droplets towards the top of the vessel (sedimentation curve). The upper curves represent the height of the completely coalesced interface (coalescence curve). The overall separation time where both

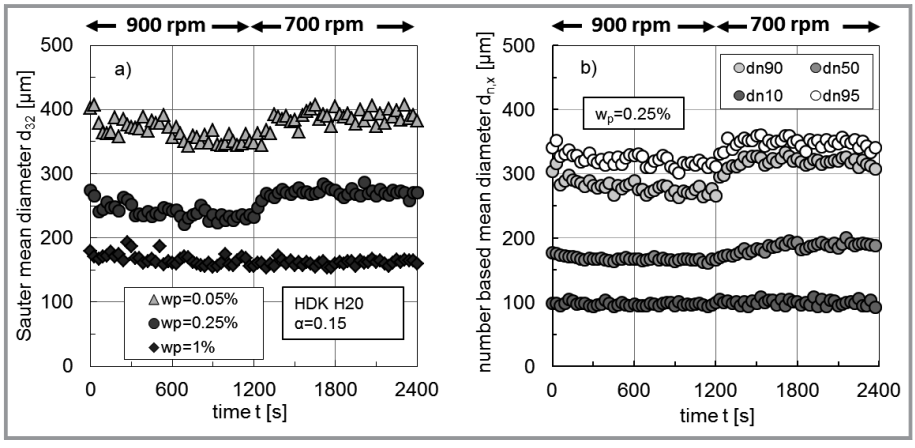

Figure 10. Dynamic behavior of the systems (HDK H20, α = 0.15, T = 293 K) for a step-wise reduction of agitation speed from 900 to 700 rpm at t = 1200 s. a) Sauter mean diameter for different particle mass fractions w_p, b) number-based diameters at w_p = 0.25 %.

curves meet was 53 s for w_p = 0.05 wt % and 117 s for the higher particle concentration of w_p = 0.15 wt %. The coalescence curves are similar and especially coalescence of the largest droplets took place within the first seconds of the separation experiments. The emulsions were only partly stabilized since the droplets were not fully coated with particles so that the phase separation was completed within several minutes or less. For particle mass fractions of w_p = 0.75 wt % and higher, the stability against coalescence rose and the phase separation took longer than 48 h. The swarm sedimentation severely decreased with rising particle mass fractions and lower droplet sizes. Fig. 11b shows the overall sedimentation speed calculated from the slope of the sedimentation curves over particle mass fraction. The shape of the curve is similar to the graph of the steady-state Sauter mean diameters over particle mass fraction in the agitated system (cf. Fig. 6a and Fig. 11b).

The swarm sedimentation speed can also be used to calculate the corresponding Sauter mean diameter of the droplet swarm and vice versa. The approach by Pilhofer and Mewes [46] assumes a mono-disperse droplet swarm and that no drop-drop coalescence occurs during sedimentation. The model is valid for Archimedes numbers of $Ar > 1$ and dispersed phase volume fractions of $0.06 < \varphi_d < 0.55$. The Reynolds number during sedimentation Re_s (Eq. (6))

$$Re_s = \frac{3\,q\,\varphi_d}{c_w \xi (1-\varphi_d)} \left(\sqrt{1 + Ar \frac{c_w \xi (1-\varphi_d)^3}{54\,q^2 \varphi_d^2}} - 1 \right) = \frac{\rho_c v_s d_{32}}{\eta_c} \tag{6}$$

is described using the Archimedes number Ar, the Hadamard-Rybczynski factor K_{HR}, the friction coefficient c_w and two coefficients ξ and q (definitions see Appendix).

The governing equations are described in detail in [44, 46] and lead to calculated Sauter mean diameters of $d_{32,wp\,=\,0.015wt\,\%}$ = 297 µm to $d_{32,wp\,=\,1.00wt\,\%}$ = 127 µm. This represents the lower size range of the drop size distributions in the agitated system measured in steady state. It should be noted that the same dispersed phase fraction as in steady state is used, since the actual values during sedimentation are unknown. For the o/w emulsions investigated in this case, the influence of the suspension viscosity was negligible. Using viscosity values at shear rates of 10 s^{-1} and 1000 s^{-1} only changes the Sauter mean diameter value in the first digit after the decimal point. For emulsions with high particle mass fractions in the continuous phase, the complex rheology should be taken into account since the swarm sedimentation model is very sensitive towards the continuous phase viscosity [46, 59]. However, this case was not investigated in this work.

5 Conclusions and Outlook

The impact of silica nanoparticles, which differ in residual silanol content or specific surface area, on drop size distributions in an agitated tank was analyzed. Physical properties that influence drop breakup and coalescence behavior were determined. All three investigated nanoparticle suspensions exhibited shear thinning flow behavior. Their yield stress increased with rising nanoparticle mass fraction and viscoelastic rheological behavior with gel character occurred. In comparison to HDK H18 and HDK H30 particles, the increase in dynamic viscosity with rising particle mass fraction is more pronounced for HDK H20 particles. The specific surface area and silanol content especially for higher particle mass fractions (w_p = 0.5–1 %) has a major impact on the liquid-particle and particle-particle interactions. No remarkable change in interfacial tension occurred for *n*-heptane suspensions with HDK H18, HDK H20 and HDK H30 against water.

The steady-state Sauter mean diameters as a function of particle mass fraction showed an impact of the hydrophobicity of the particles and their specific surface area. The decrease of the droplet size with increasing particle mass fraction was higher for HDK H20 particles in comparison to more hydrophobic particles (HDK H18) or particles with a higher specific surface area (HDK H30). The influence of the specific surface area on the drop sizes is smaller in comparison to the silanol content or the hydrophobicity of the particles. Distribution self-similarity existed for the investigated particles for one emulsion type. A comparison of the distributions of HDK H20 stabilized o/w- and w/o emulsions showed similar Sauter mean diameters, but no self-similarity of the drop size distributions. Future efforts to predict drop sizes of (partly) nanoparticle-stabilized emulsions need to include the complex rheology of the systems. Furthermore, an

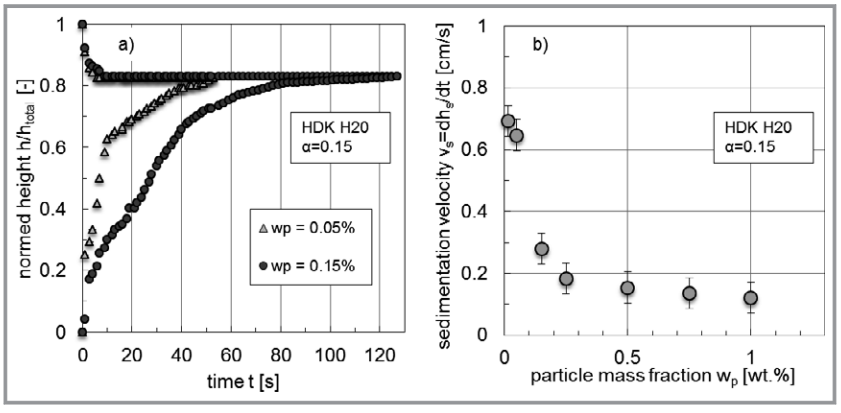

Figure 11. Batch settling results for HDK H20 stabilized emulsions after stirrer stop from 900 rpm (α = 0.15, T = 293 K). a) Coalescence and sedimentation curves over time for two nanoparticle mass fractions, b) sedimentation velocity over particle mass fraction, calculated using the slope of the sedimentation curve.

additional characterization of the system properties such as interface rigidity, particle adsorption behavior and (local) particle coverage might be needed for a comprehensive description of the systems.

We would like to thank Caroline Faller and Nina Fessler for their supportive experimental work. This work is part of the Collaborative Research Centre "Integrated Chemical Processes in Liquid Multiphase Systems" coordinated by the Technische Universitat Berlin. Financial support by the Deutsche Forschungsgemeinschaft is gratefully acknowledged (TRR 63).

Appendix

Used Equations

Circular equivalent diameter $d_{A,i}$ (m)

$$d_{A,i} = \sqrt{\frac{4\,A_i}{\pi}} \tag{A1}$$

Sauter mean diameter d_{32} (m)

$$d_{32} = \frac{\sum_{i=1}^{n} d_i^3}{\sum_{i=1}^{n} d_i^2} \tag{A2}$$

Hadamard-Rybczynski factor K_{HR}

$$K_{HR} = \frac{3(\eta_c + \eta_d)}{2\eta_c + 3\eta_d} \tag{A3}$$

Coefficient q

$$q = \frac{1 - \varphi_d}{2\varphi_d + K_{HR}} \exp\left(\frac{2.5\varphi_d}{1 - 0.61\varphi_d}\right) \tag{A4}$$

Coefficient ξ

$$\xi = 5K_{HR}^{-3/2}\left(\frac{\varphi_d}{1 - \varphi_d}\right)^{0.45} \tag{A5}$$

Friction coefficient c_w

$$c_w = \frac{Ar}{6{Re_s}^2} - \frac{3}{K_{HR}Re_s} \tag{A6}$$

Symbols used

A	[m^2]	area
Ar	[–]	Archimedes number, $\frac{\rho_c \Delta\rho g d_{32}^3}{\eta_c^2}$
c_w	[–]	friction factor
d	[m]	drop diameter
$d_{A,i}$	[m]	circular equivalent diameter
d_{10}	[m]	arithmetic mean diameter
d_{min}	[m]	minimum drop diameter
d_{max}	[m]	maximum drop diameter
$d_{n,10}$	[m]	10 % percentile value of number
$d_{n,50}$	[m]	50 % percentile value of number
$d_{n,90}$	[m]	90 % percentile value of number
$d_{n,95}$	[m]	95 % percentile value of number
$d_{v,10}$	[m]	10 % percentile value of volume
$d_{v,50}$	[m]	50 % percentile value of volume
$d_{v,90}$	[m]	90 % percentile value of volume
d_{st}	[m]	stirrer diameter
d_{32}	[m]	Sauter mean diameter
D	[m]	tank diameter
E_{ads}	[kT]	adsorption energy
f	[Hz]	frequency
F_h	[m]	height of particles
F_N	[N]	normal force
F_v	[m]	length of particles
g	[$m\,s^{-2}$]	acceleration due to gravity
G	[Pa]	shear modulus
G'	[Pa]	loss modulus
G''	[Pa]	storage modulus
h	[m]	height
h_b	[m]	baffle height
h_c	[m]	height of coalescence curve
h_{crit}	[m]	critical height of cylindrical element
h_s	[m]	height of sedimentation curve
h_{sb}	[m]	stirrer blade height
h_{st}	[m]	stirrer bottom clearance
h_{total}	[m]	total dispersion height
H	[m]	height of fluid level
K_{HR}	[–]	Hadamard-Rybczynski factor
m	[kg]	mass
n	[rpm]	agitation speed
P	[W]	power
q	[–]	coefficient
Q_0	[–]	cumulative distribution of number
Q_3	[–]	cumulative distribution of volume
R	[m]	particle radius
r_{crit}	[m]	critical radius of cylindrical element
Re_s	[–]	Reynolds number during sedimentation, $\frac{\rho_c v_s d_{32}}{\eta_c}$
s_{sb}	[m]	stirrer blade thickness
s_b	[m]	baffle thickness
t'	[s]	separation time
T	[K]	temperature
V	[m^3]	volume
v_s	[$m\,s^{-1}$]	swarm sedimentation velocity
Vi	[–]	viscosity vessel number, $\frac{\eta_c n\, d_{st}}{\sigma}\left(\frac{\rho_c}{\rho_d}\right)^{0.5}$
w_b	[m]	baffle width

w_p	[wt %]	particle mass fraction in dispersed phase
$w_{p,s}$	[wt %]	particle mass fraction in suspension
w_{sb}	[m]	stirrer blade width
We	[–]	Weber number, $\frac{\rho_c n^2 d_{st}^3}{\sigma}$

Greek letters

α	[–]	mass fraction of oil
β	[–]	aspect ratio
β_c	[–]	critical aspect ratio
γ	[%]	deformation
$\dot{\gamma}$	[s^{-1}]	shear rate
η	[Pa s]	dynamic viscosity
η_r	[–]	relative dynamic viscosity
π	[N m^{-1}]	surface pressure
ε	[W kg^{-1}]	energy dissipation rate
δ	[–]	loss factor
φ_d	[–]	dispersed phase volume fraction
θ	[°]	contact angle
σ	[N m^{-1}]	interfacial tension
σ_n	[m]	standard deviation of number
ρ	[kg m^{-3}]	density
ρ_c	[kg m^{-3}]	density of continuous phase
ρ_d	[kg m^{-3}]	density of dispersed phase
κ	[S cm^{-1}]	electrical conductivity
τ	[Pa]	shear stress
τ_0	[Pa]	yield stress
ω	[rad s^{-1}]	angular frequency
ξ	[–]	coefficient

Abbreviations

BET	Brunauer-Emmet-Teller method to determine the specific surface area
CFD	computational fluid dynamics
PBE	population balance equation
SEM	scanning electron microscopy
SiOH	residual silanol group
o/w	oil-in-water emulsion
w/o	water-in-oil emulsion
o,w	oil/water interface

References

[1] S. U. Pickering, *J. Chem. Soc.* **1907**, *91*, 2001–2021.
[2] W. Ramsden, *Proc. R. Soc.* **1903**, *72*, 156–164.
[3] A. B. Pawar, M. Caggioni, R. Ergun, R. W. Hartel, P. T. Spicer, *Soft Matter* **2011**, *7 (17)*, 7710. DOI: https://doi.org/10.1039/c1sm05457k
[4] B. P. Binks, P. D. I. Fletcher, B. L. Holt, J. Parker, P. Beaussoubre, K. Wong, *Phys. Chem. Chem. Phys.* **2010**, *12 (38)*, 11967. DOI: https://doi.org/10.1039/c0cp00581a
[5] B. P. Binks, S. O. Lumsdon, *Phys. Chem. Chem. Phys.* **2000**, *2 (13)*, 2959–2967. DOI: https://doi.org/10.1039/b002582h
[6] Y. Zhao, X. Zhang, J. Sanjeevi, Q. Yang, *J. Catal.* **2016**, *334*, 52–59. DOI: https://doi.org/10.1016/j.jcat.2015.11.011
[7] R. von Klitzing, D. Stehl, T. Pogrzeba, R. Schomäcker, R. Minullina, A. Panchal, S. Konnova, R. Fakhrullin, J. Koetz, H. Möhwald, Y. Lvov, *Adv. Mater. Interfaces* **2017**, *4 (1)*, 1600435. DOI: https://doi.org/10.1002/admi.201600435
[8] M. Petzold, S. Röhl, L. Hohl, D. Stehl, M. Lehmann, R. von Klitzing, M. Kraume, *Chem. Ing. Tech.* **2017**, *89 (11)*, 1561–1573. DOI: https://doi.org/10.1002/cite.201700060
[9] *Colloidal Particles at Liquid Interfaces* (Eds: B. P. Binks, T. S. Horozov), Cambridge University Press, Cambridge **2006**.
[10] J. Frelichowska, M.-A. Bolzinger, Y. Chevalier, *J. Colloid Interface Sci.* **2010**, *351 (2)*, 348–356. DOI: https://doi.org/10.1016/j.jcis.2010.08.019
[11] K. H. Persson, I. A. Blute, I. C. Mira, J. Gustafsson, *Colloids Surf., A* **2014**, *459*, 48–57. DOI: https://doi.org/10.1016/j.colsurfa.2014.06.034
[12] D. Stehl, L. Hohl, M. Schmidt, J. Hübner, M. Lehmann, M. Kraume, R. Schomäcker, R. von Klitzing, *Chem. Ing. Tech.* **2016**, *88 (11)*, 1806–1814. DOI: https://doi.org/10.1002/cite.201600065
[13] È. Tsabet, L. Fradette, *Chem. Eng. Res. Des.* **2015**, *97*, 9–17. DOI: https://doi.org/10.1016/j.cherd.2015.02.016
[14] S. Brunauer, P. H. Emmett, E. Teller, *J. Am. Chem. Soc.* **1938**, *60*, 309–319.
[15] B. P. Binks, J. H. Clint, *Langmuir* **2002**, *18 (4)*, 1270–1273. DOI: https://doi.org/10.1021/la011420k
[16] W. J. Tseng, K.-C. Lin, *Mater. Sci. Eng., A* **2003**, *355 (1–2)*, 186–192. DOI: https://doi.org/10.1016/S0921-5093(03)00063-7
[17] R. Mondragon, J. E. Julia, A. Barba, J. C. Jarque, *Powder Technol.* **2012**, *224*, 138–146. DOI: https://doi.org/10.1016/j.powtec.2012.02.043
[18] M. Kamibayashi, H. Ogura, Y. Otsubo, *Ind. Eng. Chem. Res.* **2006**, *45 (21)*, 6899–6905. DOI: https://doi.org/10.1021/ie0512486
[19] H. Barthel, *Colloids Surf., A* **1995**, *101*, 217–226.
[20] L. Hohl, S. Röhl, D. Stehl, R. von Klitzing, M. Kraume, *Chem. Ing. Tech.* **2016**, *88 (11)*, 1815–1826. DOI: https://doi.org/10.1002/cite.201600063
[21] S. R. Raghavan, H. J. Walls, S. A. Khan, *Langmuir* **2000**, *16 (21)*, 7920–7930. DOI: https://doi.org/10.1021/la991548q
[22] T. G. Mezger, *The Rheology Handbook*, 2nd ed., Vincentz Network, Hannover **2006**.
[23] T. Skale, L. Hohl, M. Kraume, A. Drews, *J. Membr. Sci.* **2017**, *535*, 1–9. DOI: https://doi.org/10.1016/j.memsci.2017.04.006
[24] F. Bresme, M. Oettel, *J. Phys.: Condens. Matter* **2007**, *19 (41)*, 413101. DOI: https://doi.org/10.1088/0953-8984/19/41/413101
[25] J. H. Schulman, J. Leja, *Trans. Faraday Soc.* **1953**, *50*, 598–605.
[26] W. D. Bancroft, *J. Phys. Chem.* **1913**, 501–519.
[27] R. Aveyard, B. P. Binks, J. H. Clint, *Adv. Colloid Interface Sci.* **2003**, *100–102*, 503–546. DOI: https://doi.org/10.1016/S0001-8686(02)00069-6
[28] J. Faraudo, F. Bresme, *J. Chem. Phys.* **2003**, *118 (14)*, 6518–6528. DOI: https://doi.org/10.1063/1.1559728
[29] J. O. Hinze, *AIChE J.* **1955**, *1 (3)*, 289–295. DOI: https://doi.org/10.1002/aic.690010303
[30] C. A. Coulaloglou, L. L. Tavlarides, *Chem. Eng. Sci.* **1977**, *32*, 1289–1297.
[31] R. V. Calabrese, T. P. K. Chang, P. T. Dang, *AIChE J.* **1986**, *32 (4)*, 657–666.
[32] Y. Liao, D. Lucas, *Chem. Eng. Sci.* **2010**, *65 (10)*, 2851–2864. DOI: https://doi.org/10.1016/j.ces.2010.02.020
[33] Y. Liao, D. Lucas, *Chem. Eng. Sci.* **2009**, *64 (15)*, 3389–3406. DOI: https://doi.org/10.1016/j.ces.2009.04.026

[34] S. N. Maindarkar, P. Bongers, M. A. Henson, *Chem. Eng. Sci.* **2013**, *89*, 102–114. DOI: https://doi.org/10.1016/j.ces.2012.12.001

[35] S. Maaß, N. Paul, M. Kraume, *Chem. Eng. Sci.* **2012**, *76*, 140–153. DOI: https://doi.org/10.1016/j.ces.2012.03.050

[36] J. Kamp, J. Villwock, M. Kraume, *Rev. Chem. Eng.* **2017**, *33 (1)*, 1–47. DOI: https://doi.org/10.1515/revce-2015-0071

[37] B. P. Binks, *Curr. Opin. Colloid Interface Sci.* **2002**, *7*, 21–41.

[38] I. Blute, R. J. Pugh, J. van de Pas, I. Callaghan, *Colloids Surf., A* **2009**, *337 (1–3)*, 127–135. DOI: https://doi.org/10.1016/j.colsurfa.2008.12.009

[39] H. Fan, A. Striolo, *Phys. Rev. E: Stat., Nonlinear, Soft Matter Phys.* **2012**, *86 (5 Pt 1)*, 51610. DOI: https://doi.org/10.1103/PhysRevE.86.051610

[40] S. S. Datta, H. C. Shum, D. A. Weitz, *Langmuir* **2010**, *26 (24)*, 18612–18616. DOI: https://doi.org/10.1021/la103874z

[41] Y. Chevalier, M.-A. Bolzinger, *Colloids Surf., A* **2013**, *439*, 23–34. DOI: https://doi.org/10.1016/j.colsurfa.2013.02.054

[42] T. Skale, D. Stehl, L. Hohl, M. Kraume, R. von Klitzing, A. Drews, *Chem. Ing. Tech.* **2016**, *88 (11)*, 1827–1832. DOI: https://doi.org/10.1002/cite.201600099

[43] T. Frising, C. Noïk, C. Dalmazzone, *J. Dispersion Sci. Technol.* **2006**, *27 (7)*, 1035–1057. DOI: https://doi.org/10.1080/01932690600767098

[44] M. Henschke, *Chem. Eng. J.* **2002**, *85 (2–3)*, 369–378. DOI: https://doi.org/10.1016/S1385-8947(01)00251-0

[45] S. Zeppieri, J. Rodríguez, A. L. López de Ramos, *J. Chem. Eng. Data* **2001**, *46 (5)*, 1086–1088. DOI: https://doi.org/10.1021/je000245r

[46] T. Pilhofer, D. Mewes, *Siebboden-Extraktionskolonnen*, Verlag Chemie GmbH, Weinheim **1979**.

[47] S. Wollny, *Experimentelle und numerische Untersuchungen zur Partikelbeanspruchung in gerührten (Bio-)Reaktoren*, Dissertation, Technische Universität Berlin **2010**.

[48] Q. Nguyen, *Ann. Rev. Fluid Mech.* **1992**, *24 (1)*, 47–88. DOI: https://doi.org/10.1146/annurev.fluid.24.1.47

[49] T. Okubo, *J. Colloid Interface Sci.* **1995**, *171*, 55–62.

[50] V. R. Dugyala, J. S. Muthukuru, E. Mani, M. G. Basavaraj, *Physical chemistry chemical physics PCCP* **2016**, *18 (7)*, 5499–5508. DOI: https://doi.org/10.1039/c5cp05959c.

[51] S. Kutuzov, R. Tangiarala, T. Emrick, T. P. Russell, A. Böker, *Physical chemistry chemical physics PCCP* **2007**, *9 (48)*, 6351–6358. DOI: https://doi.org/10.1039/b705094a.

[52] N. Bizmark, M. A. Ioannidis, D. E. Henneke, *Langmuir* **2014**, *30 (3)*, 710–717. DOI: https://doi.org/10.1021/la404357j

[53] N. Glaser, D. J. Adams, A. Böker, G. Krausch, *Langmuir* **2006**, *22 (12)*, 5227–5229. DOI: https://doi.org/10.1021/la060693i

[54] R. Aveyard, J. H. Clint, D. Nees, V. N. Paunov, *Langmuir* **2000**, *16 (4)*, 1969–1979. DOI: https://doi.org/10.1021/la990887g

[55] T. S. Horozov, B. P. Binks, R. Aveyard, J. H. Clint, *Colloids Surf., A* **2006**, *282–283*, 377–386. DOI: https://doi.org/10.1016/j.colsurfa.2005.11.085

[56] S. Maaß, J. Rojahn, R. Hänsch, M. Kraume, *Comput. Chem. Eng.* **2012**, *45*, 27–37. DOI: https://doi.org/10.1016/j.compchemeng.2012.05.014

[57] C. P. Whitby, E. J. Wanless, *Materials* **2016**, *9 (8)*, 626. DOI: https://doi.org/10.3390/ma9080626

[58] M. Kraume, A. Gäbler, K. Schulze, *Chem. Eng. Technol.* **2004**, *27 (3)*, 330–334. DOI: https://doi.org/10.1002/ceat.200402006

[59] L. Hohl, V. Röder, M. Kraume, *Chem. Eng. Technol.* **2019**, *42 (8)*, 1574–1586. DOI: https://doi.org/10.1002/ceat.201800743

[60] B. P. Binks, S. O. Lumsdon, *Langmuir* **2000**, *16 (23)*, 8622–8631. DOI: https://doi.org/10.1021/la000189s

